Stanford Exploration Project, Report 115, May 22, 2004, pages **??***–108*

Least-squares joint imaging of multiples and primaries applied to 3-D field data

Morgan Brown[1]

ABSTRACT

In this paper I outline the extension to 3-D of the Least-squares Joint Imaging of Multiples and Primaries (LSJIMP) method for simultaneously separating multiples and primaries and combining their information. I apply LSJIMP to a 3-D field dataset and demonstrate that the method cleanly removes surface-related multiples from the data while preserving the prestack amplitude signature of the primaries. LSJIMP compares favorably to least-squares Radon demultiple, both in terms of computational performance and result quality.

INTRODUCTION

Multiple reflections often erect the highest barrier to the successful imaging and interpretation of marine seismic data. Despite their nuisance, however, multiples illuminate the prospect zone, and moreover, illuminate different angular ranges and reflection points than primaries. In theory and in practice, multiples provide subsurface information that primaries do not. To use the information in the multiples, we must map multiples and primaries to a domain where they are comparable, like a prestack image domain, and then combine them.

The semi-independent measurements provided by primaries and multiples overlap each other in one data record. In theory, averaging the multiple and primary images can improve signal fidelity and fill coverage gaps, but this encounters two problems in practice. First, unless we correct multiples for their different raypaths and additional reflections, the signal events are incomparable. Secondly, just as multiples represent noise on the primary image, primaries and higher order multiples represent noise on a first-order multiple image. Corresponding noise, or "crosstalk" events on the images are often kinematically consistent, so adding the images may actually degrade signal fidelity. Prestack separation of multiples and primaries is a prerequisite to image averaging.

I presented the LSJIMP method to simultaneously solve the separation and integration problems, as a global inversion (Brown, 2003b). The model space is a collection of images, with the energy from each mode partitioned into only one image. The forward model contains amplitude corrections which ensure that the signal events in the multiple and primary images

[1]**email:** morgan@sep.stanford.edu

are directly comparable, in terms of both kinematics and amplitudes. I presented an efficient kinematic (Brown, 2003c) and amplitude (Brown, 2003a) modeling scheme which combines the efficiency necessary to realistically run on real 3-D data with the accuracy to model pegleg multiples in a moderately complex earth. Three model regularization operators exploit multiplicity between and within the images to discriminate between crosstalk and signal, combine the images, fill coverage gaps, and increase signal fidelity.

I previously applied LSJIMP to a difficult 2-D Gulf of Mexico data example (Brown, 2003b). In this paper, I apply LSJIMP to a 3-D data example, also from the Gulf of Mexico. CGG donated the data, which were acquired in Green Canyon. I demonstrate that LSJIMP can cleanly separate the multiples and primaries in the data, in spite of sparse data geometry that inhibits many other multiple suppression techniques. I show that LSJIMP compares favorably to least-squares Radon demultiple, both in terms of computational performance and result quality. Last, I show that the LSJIMP estimated primaries are more robust with respect to amplitude-versus-offset (AVO) analysis than the raw data.

LSJIMP REVIEW

LSJIMP models the recorded data as the sum of primary reflections and p orders of pegleg multiples from n_{surf} multiple generators. An i^{th}-order pegleg splits into $i+1$ legs. Denoting the primaries $\mathbf{d}_0$ and the k^{th} leg of the i^{th} order pegleg from the m^{th} multiple generator $\mathbf{d}_{i,k,m}$, the modeled data takes the following form:

$$\mathbf{d}_{\text{mod}} = \mathbf{d}_0 + \sum_{i=1}^{p} \sum_{k=0}^{i} \sum_{m=1}^{n_{\text{surf}}} \mathbf{d}_{i,k,m}. \tag{1}$$

If we have designed imaging operators that map primaries and multiples to comparable signal events (kinematics and angle-dependent amplitudes), we can write the $\mathbf{d}_{i,k,m}$ as linear functions of prestack images. We can similarly denote the modeling operators (adjoint to imaging) for primaries and peglegs as $\mathbf{L}_0$ and $\mathbf{L}_{i,k,m}$, respectively, and the images of the primaries and peglegs as $\mathbf{m}_0$ and $\mathbf{m}_{i,k,m}$, respectively. Rewriting equation (1), we have:

$$\mathbf{d}_{\text{mod}} \;=\; \mathbf{L}_0\mathbf{m}_0 + \sum_{i=1}^{p} \sum_{k=0}^{i} \sum_{m=1}^{n_{\text{surf}}} \mathbf{L}_{i,k,m}\mathbf{m}_{i,k,m} \;=\; \mathbf{L}\mathbf{m} \tag{2}$$

The LSJIMP method optimizes the primary and multiple images, $\mathbf{m}$, by minimizing the ℓ_2 norm of the difference between the recorded data, $\mathbf{d}$, and the modeled data, $\mathbf{d}_{\text{mod}}$:

$$\min_{\mathbf{m}} \; \|\mathbf{d} - \mathbf{L}\mathbf{m}\|^2. \tag{3}$$

Minimization (3) is under-determined for most choices of $\mathbf{L}_0$ and $\mathbf{L}_{i,k,m}$, implying infinitely many solutions. Crosstalk leakage is a symptom of the problem. For instance, $\mathbf{L}_0$ maps residual first-order multiple energy in $\mathbf{m}_0$ to the position of a first-order multiple in data space. Minimization (3) alone cannot distinguish between crosstalk and signal. Without model regularization, the basic LSJIMP problem is intractable.

Previously (Brown, 2003b), I devised discriminants between crosstalk and signal, and used them to derive three model regularization operators which choose the set of primary and multiple images which are optimally free of crosstalk. Moreover, these operators exploit signal multiplicity–within and between images–to increase signal fidelity, fill coverage gaps, and combine multiple and primary information. These model regularization operators are the key to the LSJIMP method's novelty.

To solve the regularized LSJIMP problem, we supplement minimization (3) with the three model regularization operators:

$$\min_{\mathbf{m}} \|\mathbf{Lm}-\mathbf{d}\|^2 + \epsilon_1^2\|\mathbf{r}_m^{[1]}\|^2 + \epsilon_2^2\|\mathbf{r}_m^{[2]}\|^2 + \epsilon_3^2\|\mathbf{r}_m^{[3]}\|^2. \tag{4}$$

$\mathbf{r}_m^{[1]}$, $\mathbf{r}_m^{[2]}$, and $\mathbf{r}_m^{[3]}$ are the model residuals corresponding to differencing across images, differencing across offset, and crosstalk penalty weighting, respectively. Scalars ϵ_1, ϵ_2, and ϵ_3 balance the relative weight of the three model residuals with the data residual. I use the conjugate gradient method for minimization (4).

Previously (Brown, 2003c,a), I outlined an efficient prestack, true relative amplitude imaging scheme for pegleg multiples. We can rewrite $\mathbf{L}_{i,k,m}$ as the cascade of a differential geometric spreading correction for multiples ($\mathbf{G}_{i,m}$), Snell Resampling to normalize a multiple's AVO to its primary ($\mathbf{S}_{i,m}$), HEMNO (Heterogeneous Earth Multiple NMO Operator) to kinematically image split peglegs ($\mathbf{N}_{i,k,m}$), and finally, application of the multiple generator's spatially-variant reflection coefficient ($\mathbf{R}_{i,k,m}$):

$$\mathbf{L}_{i,k,m} = \mathbf{R}_{i,k,m}\mathbf{N}_{i,k,m}\mathbf{S}_{i,m}\mathbf{G}_{i,m}. \tag{5}$$

The imaging operator for primaries, $\mathbf{L}_0$, is simply NMO. The imaged multiples and primaries on the $\mathbf{m}_{i,k,m}$ in equation (2) are directly comparable in terms of kinematics and amplitudes. We can exploit this important fact (with model regularization) to discriminate crosstalk from signal, and also to spread information between the images. A true relative amplitude imaging scheme like equation (5) is crucial to fully leverage the multiples in this joint imaging algorithm. Since we apply the operator and its adjoint many times in iterative optimization, computational efficiency is crucial. Because HEMNO images (like NMO) by vertical stretch, equation (5) is fast, memory-conserving, and robust to poorly sampled wavefields, which are the norm with 3-D acquisition. Brown and Guitton (2004) demonstrated that this modeling/imaging approach can accurately model multiples, even in a moderately complex earth.

3-D THEORY

In marine environments, three-dimensional reflection seismic data is normally acquired in a so-called "wide tow" streamer configuration, illustrated in Figure **??**. Ironically, the crossline azimuth range of this data is less than with most land acquisition geometries, so geophysicists often call towed streamer data "narrow azimuth" data. Note that the crossline shot interval, Δs_y, is chosen such that the outermost receiver line on one swath overlaps the innermost receiver line on the previous swath. Figure **??** illustrates that such an acquisition geometry

produces a regularly sampled crossline CMP axis, if cable feathering is absent. In one sense, this geometry boasts some degree of optimality, as it produces a well-sampled 3-D image at a minimum cost.

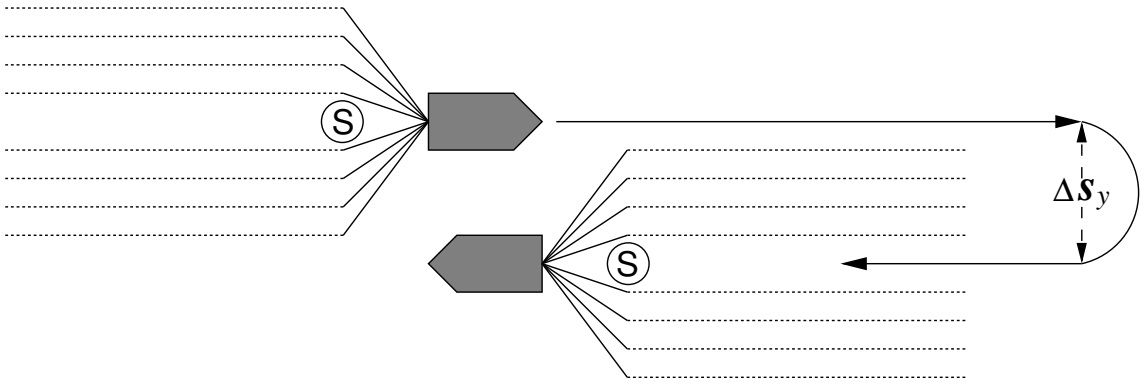

Figure 1: Wide tow marine geometry. The acquisition boat tows many (usually 4-12) receiver lines and steams in parallel sail lines. morgan1-narrow-az [NR]

Unfortunately, geometry shown in Figure **??** causes the 3-D extension of the SRME method of multiple prediction to fail spectacularly. SRME requires Δs_y to be relatively small–in practice, roughly the same as commonly chosen crossline receiver line spacing parameters (**?**). 3-D field datasets commonly have a crossline shot interval of up to ten times the crossline receiver line spacing. Workarounds for the 3-D sampling problem include: ignoring crossline structure and using a 2-D prediction, massive (270,000 CPU hours) shot interpolation (**?**), sparse inversion of the crossline multiple contribution gathers (van Dedem and Verschuur, 2002; **?**), and novel acquisition geometries (**?**). Currently, none of these methods combines proven accuracy with computational/cost efficiency.

LSJIMP AND WIDE TOW MARINE DATA

For the particular geometry shown in Figures **??** and **??**, notice that each crossline midpoint gather is occupied by one, and only one receiver line. Therefore, we can conceptualize a 3-D CMP gather as a 2-D CMP gather with nonzero crossline offset, and thus remove the crossline offset axis from five-dimensional CMP-sorted data, saving considerable memory and computational waste. This approach is similar in spirit to Biondi's (1997) combination of azimuth moveout (AMO) (Biondi et al., 1998) and common-azimuth wave equation depth migration (Biondi and Palacharla, 1996) for the prestack imaging of primaries in data with narrow-azimuth geometries. Unfortunately, the AMO transformation is not generally valid for multiples.

HEMNO is well-suited to image multiples with the data geometry described above, primarily because HEMNO images pegleg multiples with a vertical time shift. Rather than correlating wavefields across possibly-undersampled axes like migration, HEMNO uses a measurement of the data's zero-offset time dip to account for structure-induced moveout variations.

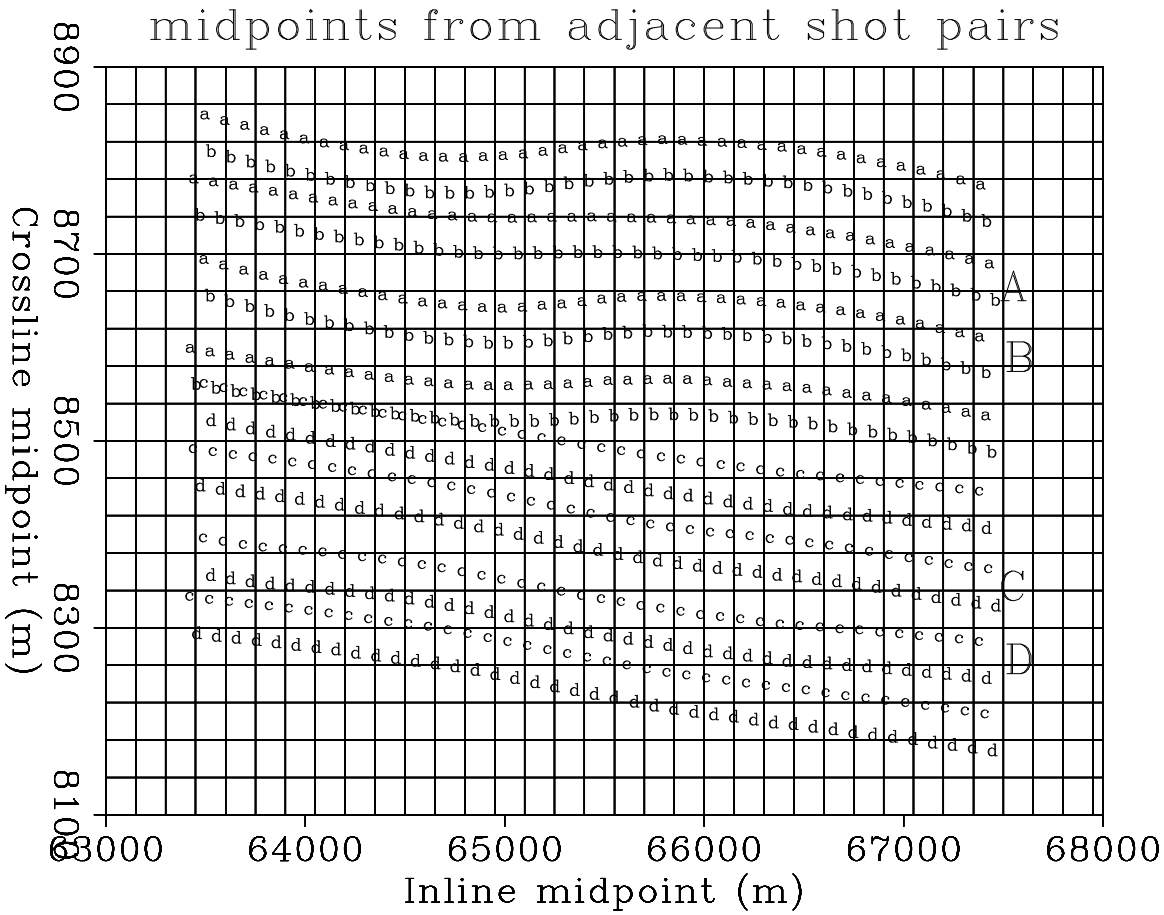

Figure 2: Midpoint locations from two adjacent sail lines of the CGG Green Canyon 3-D dataset. The boat tows four streamers and fires two sources alternatively in a "flip-flop" configuration. Midpoints from shot "A" are labeled "a", and so on. Two shot pairs from each sail line are shown. For a fixed ship speed, this geometry doubles crossline midpoint density, at the cost of reduced inline resolution, compared to a single-source configuration. Flip-flop shooting allows one airgun to be recharged while the other shoots, thereby allowing the ship to sail faster than would be possible with one gun. Cable feathering is evident, though not severe. morgan1-cgg-midpoints [NR]

Because the crossline offset axis is removed, the computational cost increase of applying HEMNO to 3-D data versus 2-D data is only proportional to the number of crossline midpoints.

My particular LSJIMP implementation, outlined in two previous works (Brown, 2003c,a), uses HEMNO, an extension of the NMO equation for multiples, in conjunction with three amplitude normalization operators to produce a "true relative amplitude" image of pegleg multiples. One of these, the Snell Resampling operator, moves multiple energy across offset to make the multiple's AVO response comparable to its primary. However, the use of Snell Resampling in the crossline direction on narrow azimuth data runs contrary to the stated assumption that we store only one crossline offset bin per 3-D CMP gather. Therefore, for the results shown in this paper, I do not apply crossline Snell Resampling. In practice, little useful angular information is anyway obtained in the crossline direction, since in most cases the data will have a maximum crossline offset of only a few hundred meters.

CGG GREEN CANYON IV 3-D DATA

In 2003, CGG donated a large portion of a 161-block speculative seismic survey it acquired in the Green Canyon region of the Gulf of Mexico. The data were acquired in the transition zone between the edge of the Continental Shelf and the Sigsbee escarpment which signals the edge of the abyssal plain. Geologically, the Green Canyon region is characterized by sedimentary "minibasins" interrupted by complex salt bodies (**?**).

CGG's 3-D data were acquired by a ship sailing east-to-west, in the strike direction relative to the dominant geologic dip. The subset of the data that I process in this paper contains fairly significant crossline dip ($> 3^\circ$) in most places. Figure **??** shows a stacked section of the subset, which contains 192 midpoints inline and 14 midpoints crossline. The stacked section includes contributions from two adjacent sail lines, the geometries of which are illustrated in Figure **??**.

The subset shown in Figure **??** is situated in a sedimentary minibasin, with strong reflections visible at a two-way traveltime of well over 5 seconds. Thanks to a strong velocity gradient and the sparse offset sampling, surface-related multiples are largely absent from the stacked section. Still, as we shall see, the multiples are fairly strong in the prestack data and inhibit prestack amplitude analysis. The section exhibits moderate reflector dip – an anticlinal structure in the inline direction and effectively constant crossline dip of several degrees.

The acquisition ship sailed quite fast, with a flip-flop source interval of 37.5 meters, and an interval of 75 meters between like sources. The fast ship speed leads to reduced resolution along the inline offset axis: for an 8100-meter cable with receiver group spacing of 25 meters, the nominal CMP fold is only 54, implying a nominal inline offset spacing of 150 meters. Figure **??** illustrates the sparse sampling of the inline offset axis. While the nominal inline offset bin size of 150 meters ensures that all bins will contain a live trace, such sparsity will greatly inhibit the estimation of reasonable stacking velocities and create "checkerboard" artifacts in the shallow portions of a stacked image.

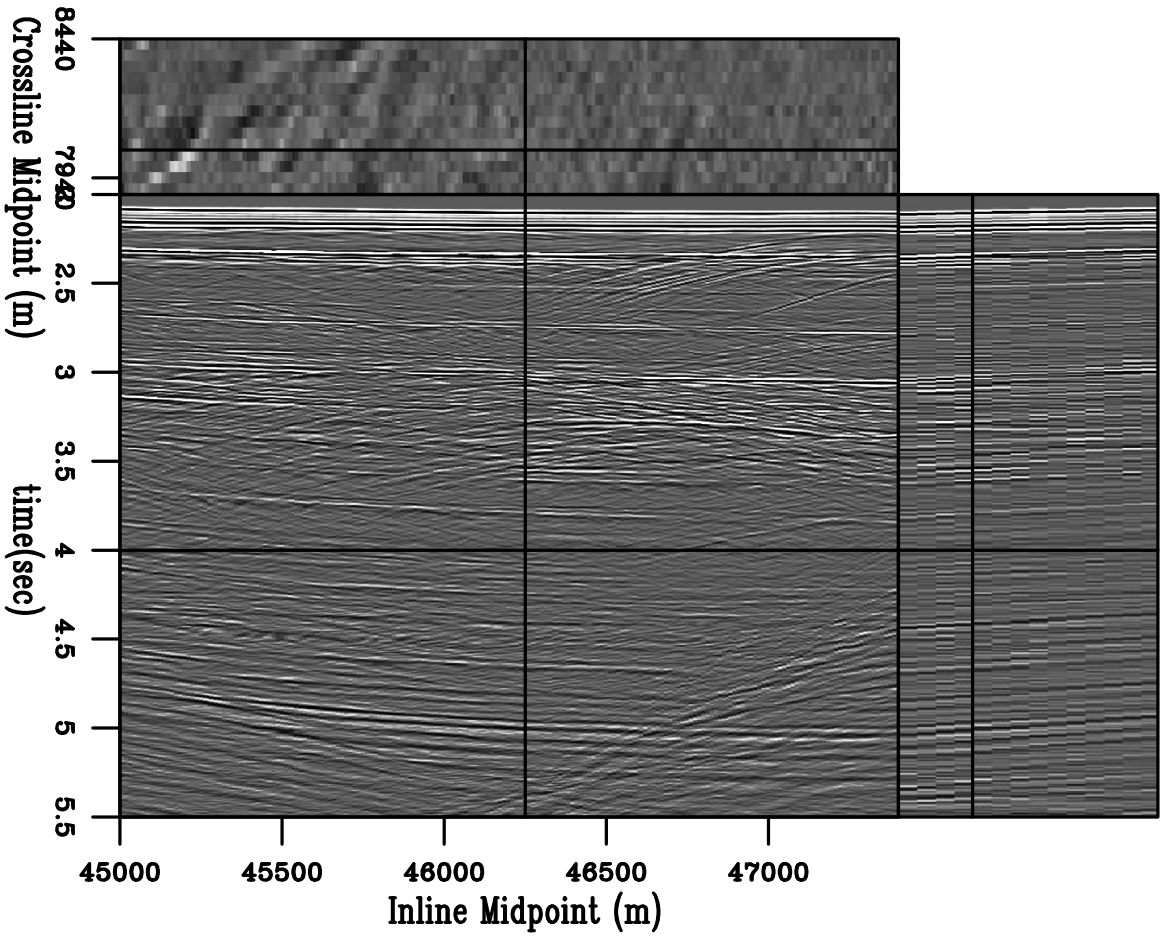

Figure 3: Stacked section of subset of Green Canyon IV 3-D dataset. morgan1-stackraw3d.gc3d [ER]

Therefore, in my processing of this dataset, I use an offset bin spacing of 25 meters. While this fine sampling better honors the physics of the experiment, it leads to a fivefold increase in empty bins. Moreover, although I have cast LSJIMP primarily as a wavefield separation algorithm, recall that one major motivation of integrating multiples and primaries is to use the multiples as a constraint on the primaries in zones where we do not record data. Multiples sample reflectors more finely in reflection angle/offset than do primaries. Moreover, the regularization strategies discussed earlier provide the infrastructure to exploit the inherent multiplicity of signal within an image and between multiple and primary images. Although designed to separate signal and noise, these same strategies also prove adept at interpolating signal in missing traces.

Stacking velocities were computed by a conventional velocity scan, coupled with maximum amplitude autopicking and local weighted (stack power) mean smoothing. The residual weight, simply zero for missing traces, but one elsewhere, is particularly important to achieve a successful LSJIMP result.

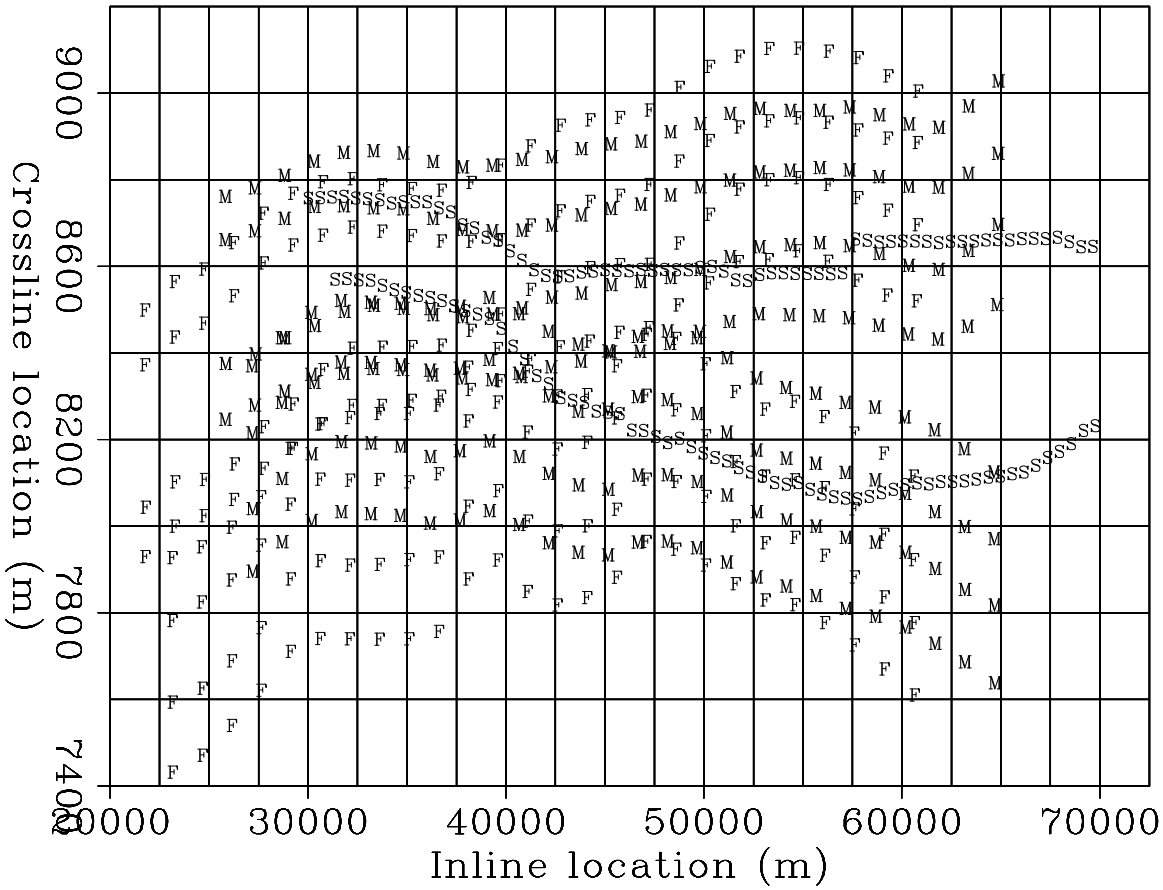

Figure 4: Acquisition geometry for two sail lines contributing to subset shown in Figure **??**. "S" symbols illustrate source positions. "M" and "F" symbols illustrate the medium- and far-offset receivers, respectively, on each of the boat's four streamers. The nominal sail line spacing is 300 meters, although it varies considerably in this case from about 200 to 500 meters. The subset processed in this section contains shot records from about 40,000 to 50,000 meters inline location. Cable feathering in this zone is present, though not severe. The two sail lines overlap to some extent, which reduces the number of crossline midpoint locations from these two sail lines to 14 from 16 over the subset. morgan1-feather [NR]

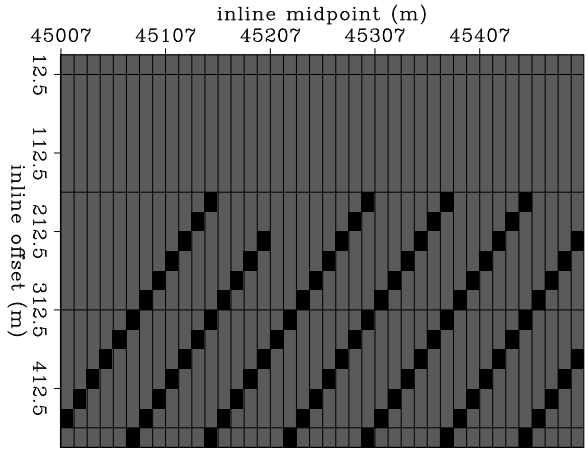

Figure 5: Illustration of sparsity of inline offset axis of CGG Green Canyon IV data. Grid represents nominal bin size of 150x12.5 meters. Black dots correspond to trace locations. morgan1-sparse.gc3d [ER]

RESULTS

Figure **??** shows stacked sections from the multiple-infested zone of the CGG subset before and after application of LSJIMP. Figure **??** is in the same format, but shows a zoom of the multiple-infested region. CMP stacking strongly suppresses the multiples, but from the difference panel, notice that LSJIMP has nonetheless subtracted most of the remaining surface-related multiple energy, and has preserved the stronger primaries to a great extent. The time-slice on the 3-D cube transects the seabed pegleg from reflector R1; it shows up prominently on the raw data stack, as well as on the difference panel, but has been largely suppressed from the LSJIMP estimated primaries stack.

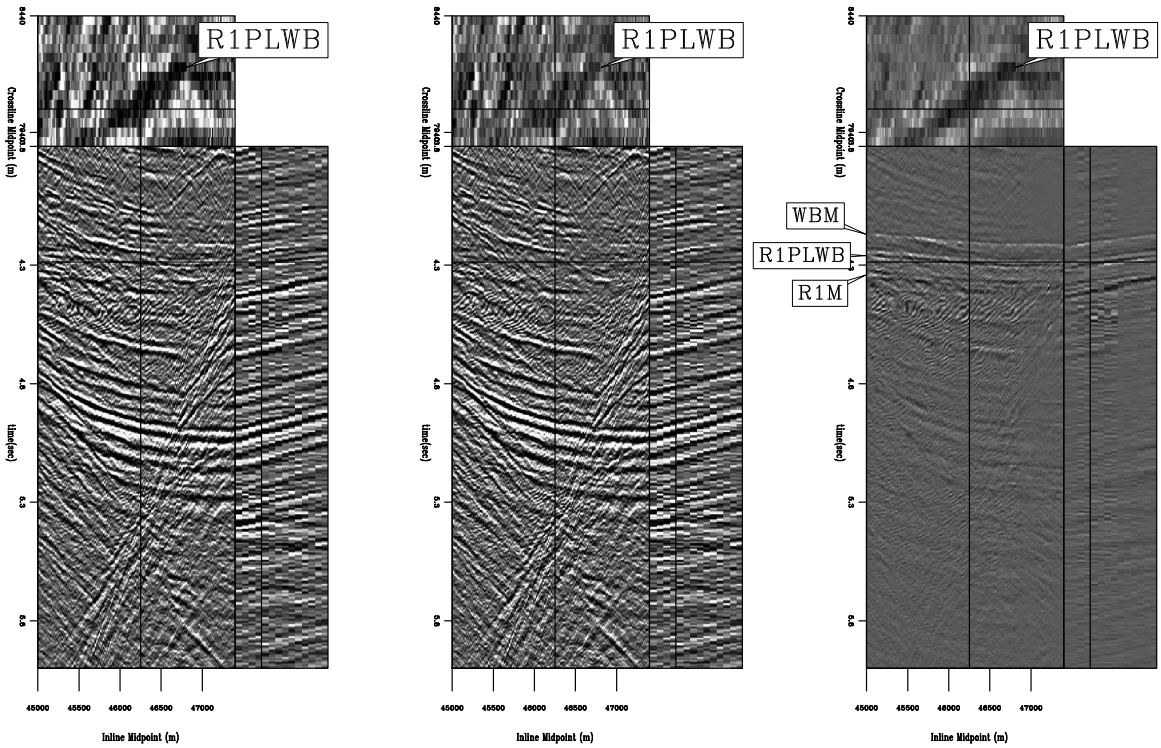

Figure 6: Stacked subset (192 midpoints inline, 14 midpoints crossline) of CGG 3-D data before and after LSJIMP. All panels windowed in time from 3.8 to 6.0 seconds and gained with t^2. Left: Raw data stack. Center: Stack of estimated primary image, $\mathbf{m}_0$. Right: Stack of the subtracted multiples. Naming convention for pure first-order multiples: (*reflector*)M, e.g., R1M. Naming convention for first-order pegleg multiples: (*target*)PL(*multiple generator*), e.g., R1PLWB. morgan1-stackcomp3d.gc3d [CR,M]

Figures **??** and **??** illustrate LSJIMP's performance on two individual CMP gathers extracted from different portions of the CGG 3-D data. It is in this domain where the strength of the LSJIMP method shines most. The raw data panels show strong surface-related multiples with an onset of around 4.3 seconds, and also fairly strong primary events under the curtain of multiples. The LSJIMP estimated primaries in panel (b) are effectively free of multiples, and moreover, since the data residual panel (f) barely contains any noticeable flat primary en-

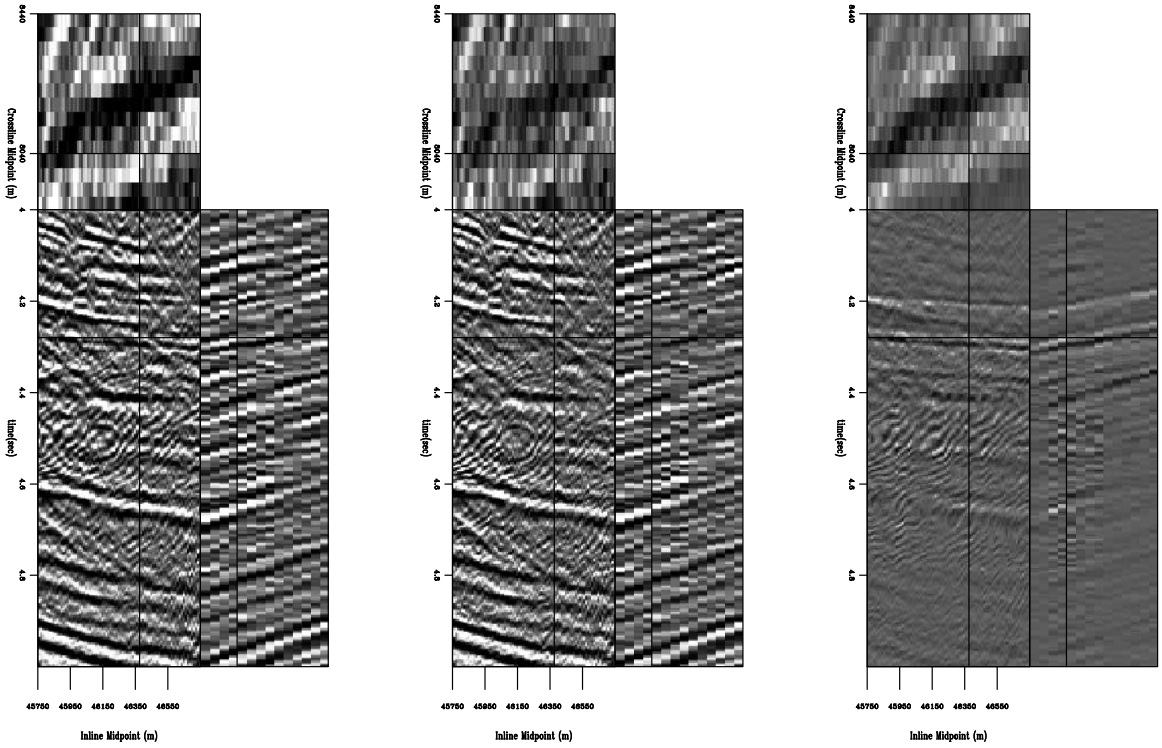

Figure 7: Zoom of stacked subset of CGG 3-D data before and after LSJIMP. All panels windowed in time from 4.0 to 5.0 seconds. Left: Raw data stack. Center: Stack of estimated primary image, $\mathbf{m}_0$. Right: Stack of the subtracted multiples. morgan1-stackcomp3d.zoom.gc3d [CR,M]

ergy, we have preserved the primary events. Also notice that the data residual contains little structured energy. This implies that the LSJIMP forward model accurately models the primaries and important multiples in the data. Unfortunately, much of this "unstructured" energy likely belongs to fairly weak pegleg multiples that simply appear incoherent with the data's poor inline resolution. On Figure **??**, notice that cable feathering has caused missing traces at far offsets. LSJIMP has used the data's multiplicity and model constraints to reasonably extrapolate the missing traces.

LSJIMP versus Radon Demultiple

Radon demultiple remains the default multiple suppression technique in many situations, particularly in 3-D, where acquisition sparsity may inhibit other techniques. On CMP gathers, primaries and multiples normally have different apparent velocities, and a Radon transform which sums across offset using various curvature parameters will focus the two types of events in different parts of the transform panel. The most natural curvature parameter for CMP data is the velocity of the hyperbola defined by the NMO equation (Foster and Mosher, 1992). While the Hyperbolic Radon transform is a linear mapping, it is not time-invariant, and thus cannot be implemented efficiently as a Fourier domain operator. However, a multiple's resid-

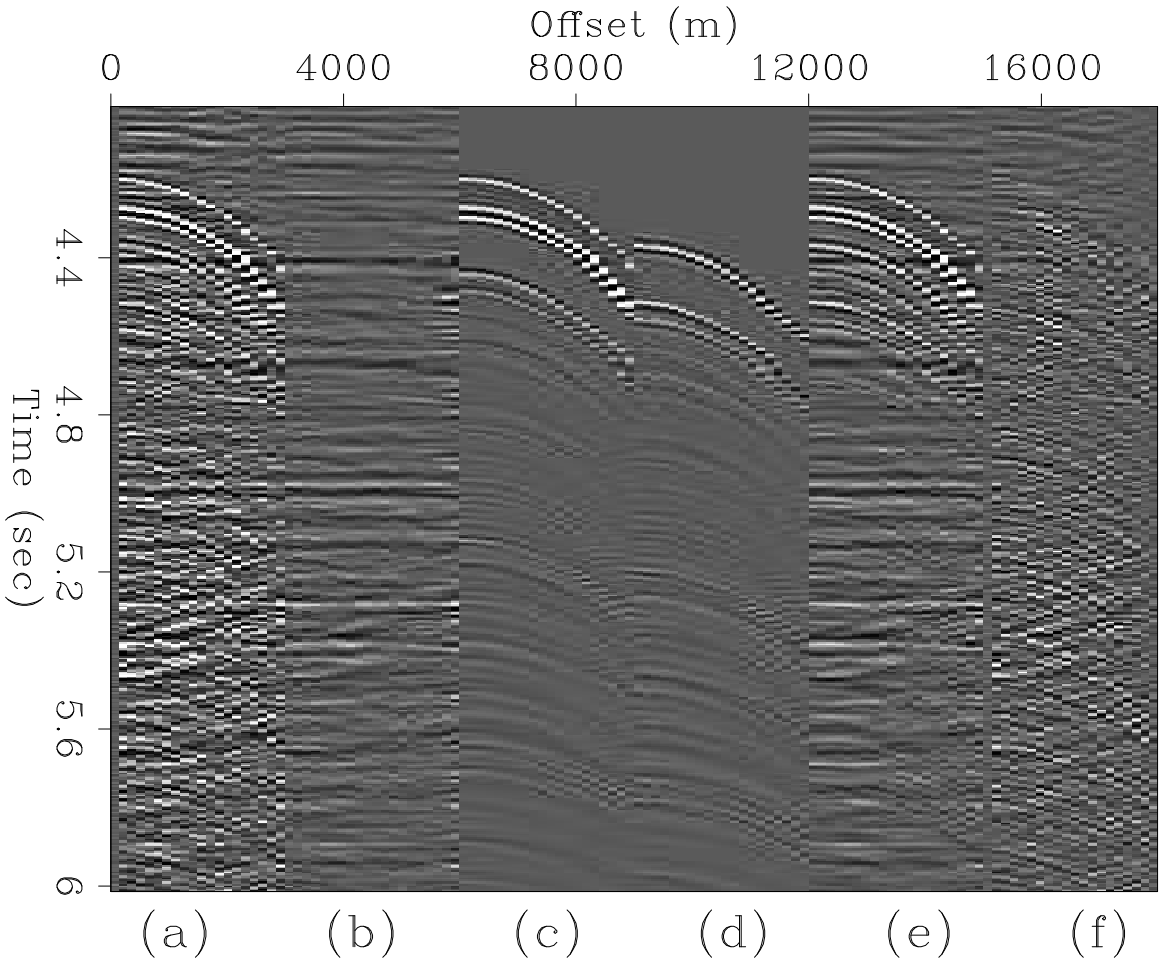

Figure 8: LSJIMP results on individual midpoint location (CMPx=100,CMPy=4). All panels decimated in offset by a factor of 6 and NMO'ed with stacking velocity, for display purposes. Panel (a): Raw data. Panel (b): LSJIMP estimated primaries. Panels (c) and (d): Estimated seabed and R1 pegleg multiples. Panel (e): Modeled data (sum of panels (b), (c), and (d)). Panel (f): Data residual (difference of panels (a) and (e)), with residual weight applied. morgan1-compwind.lsrow.gc3d.100.4 [CR]

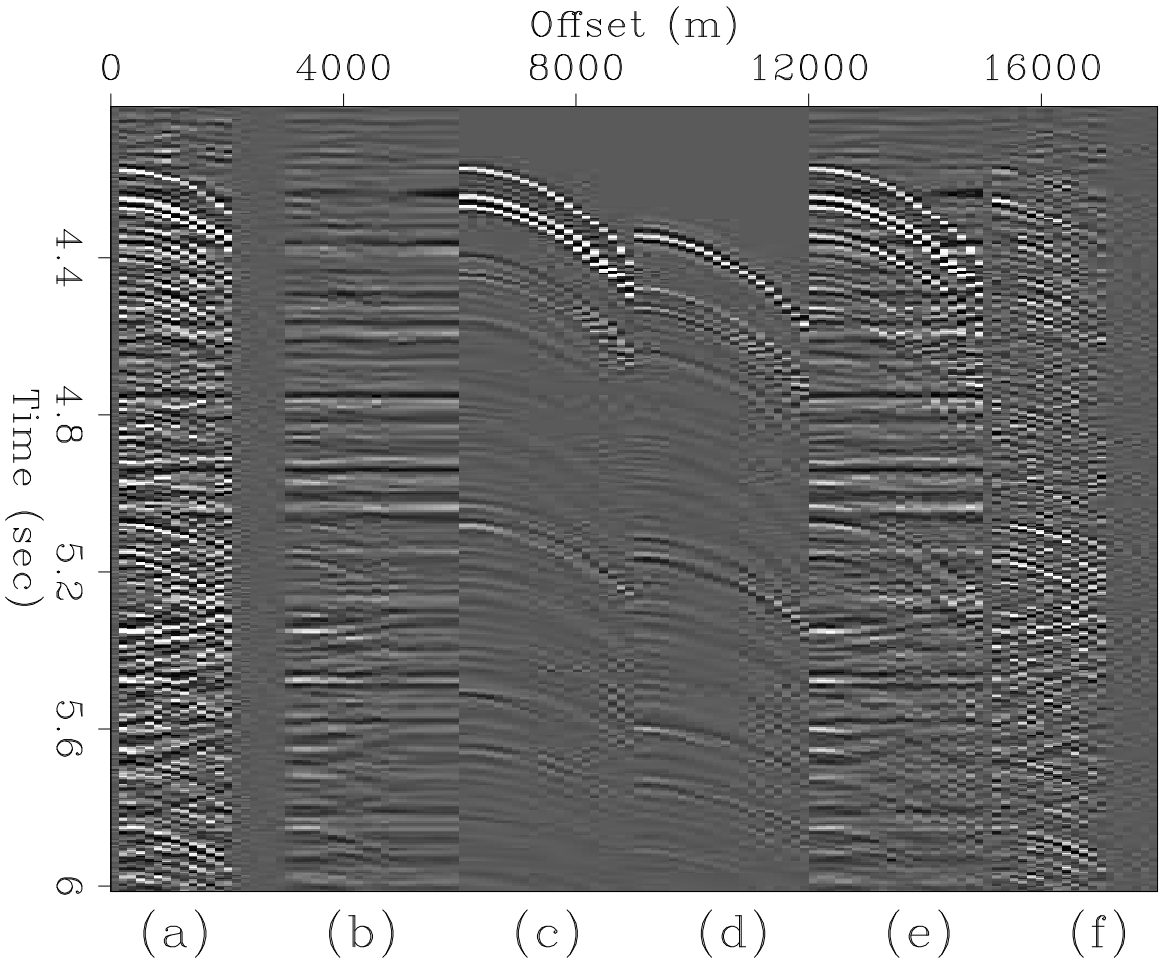

Figure 9: LSJIMP results on individual midpoint location (CMPx=100,CMPy=12). All panels decimated in offset by a factor of 6 and NMO'ed with stacking velocity, for display purposes. Panel (a): Raw data. Panel (b): LSJIMP estimated primaries. Panels (c) and (d): Estimated seabed and R1 pegleg multiples. Panel (e): Modeled data (sum of panels (b), (c), and (d)). Panel (f): Data residual (difference of panels (a) and (e)), with residual weight applied. morgan1-compwind.lsrow.gc3d.100.12 [CR]

ual moveout after NMO is approximately parabolic (quadratic) with offset, so a time-invariant Parabolic Radon transform is much faster, though not as accurate (Hampson, 1986; Kabir and Marfurt, 1999).

To remove multiples, the multiple energy in the transform panel is muted, and the inverse Radon transform applied to produce multiple-free CMP data. If we define $\mathbf{d}$ as a raw CMP gather, $\mathbf{H}$ as the linear mapping between Radon transform space and data space, $\mathbf{M}$ as a mute operator that zeroes multiple energy in Radon transform space, and $\mathbf{d}_r$ as the estimated primaries, then we can express the Radon demultiple process in equation form:

$$\mathbf{d}_r = \mathbf{H}\mathbf{M}^T\mathbf{H}^T\mathbf{d}. \tag{6}$$

Operator $\mathbf{H}$ is non-unitary ($\mathbf{H}^T\mathbf{H} \neq \mathbf{I}$), so the amplitude of the estimated primaries will not match the recorded primaries. By casting Radon demultiple as a least-squares optimization problem, the Radon transform panel can be scaled such that $\mathbf{d}_r$ and $\mathbf{d}$ are directly comparable. We first optimize a Radon transform panel, $\mathbf{p}$, to minimize the data misfit:

$$\min_{\mathbf{p}} Q(\mathbf{p}) = \|\mathbf{H}\mathbf{p} - \mathbf{d}\|^2, \tag{7}$$

and then apply the mute operator and adjoint of $\mathbf{H}$ to produce the estimated primaries:

$$\mathbf{d}_r = \mathbf{H}\mathbf{M}^T\mathbf{p}. \tag{8}$$

The finite frequency content of the data, limited extent of the array, and the intrinsic unresolvability of velocity information at zero offset all contribute to the non-uniqueness of the least-squares Radon demultiple problem. At far offsets, events with many zero-offset traveltimes and different velocities are fit equally well by a single curvature parameter. Low-frequency data makes moveout discrimination between multiples and primaries more difficult. At near offsets, all the events are fit equally well by all curvature parameters. All these pitfalls lead to reduced resolution of events in the Radon domain. So-called "high resolution" least-squares Radon transform implementations partially overcome these problems by imposing sparsity constraints in either the hyperbolic or parabolic Radon domain (Thorson and Claerbout, 1985; Sacchi and Ulrych, 1995).

I implemented and tested least-squares Hyperbolic Radon demultiple (LSHRTD) on the CGG 3-D data subset. I performed 10 conjugate gradient iterations to produce an optimal $\mathbf{p}$, then applied a mute function which is zero for velocities less than 85% and greater than 115% of the known stacking velocity. The mute tapers linearly from 0.0 to 1.0 at 90% and 110% of the known stacking velocity, respectively. The computational cost of LSHRTD is very similar to the cost of applying LSJIMP.

Figure **??** compares the results of applying LSJIMP and LSHRTD on a single CMP gather from the CGG 3-D data (CMPx=100, CMPy=4). The LSHRTD results are quite good, as we expect, given the high velocity gradient and relatively simple moveout seen in this region of the data. Note some "smearing" of primaries in the LSHRTD result, as well as a generally higher level of energy removed from the data. Both effects would likely be lessened by a more conservative, tapered mute. LSJIMP is a more "surgical" separation technique, although

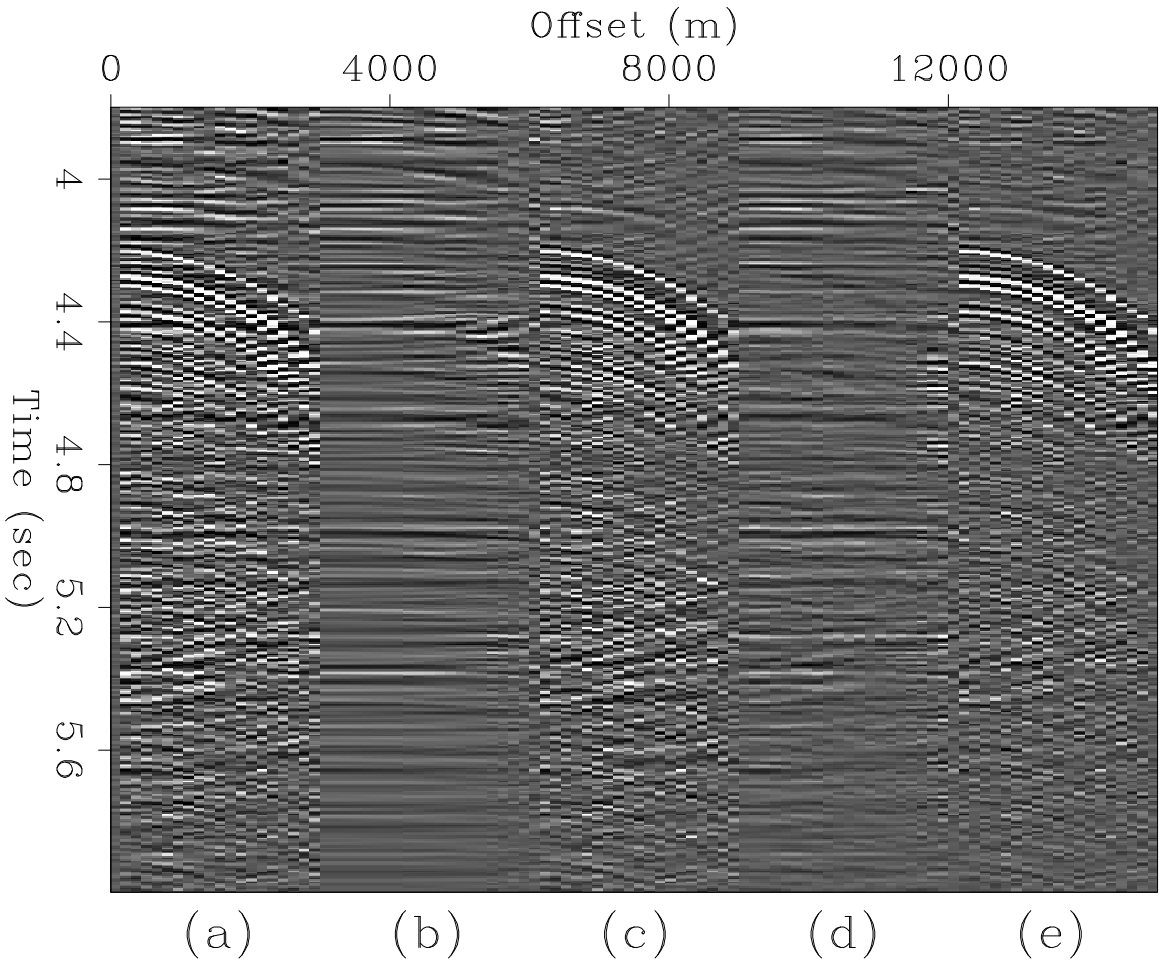

Figure 10: LSJIMP versus least-squares Hyperbolic Radon demultiple (LSHRTD) on one CMP gather of the CGG 3-D dataset. Panel (a): Raw data. Panel (b): LSHRTD estimated primaries. Panel (c): LSHRTD estimated multiples. Panel (d): LSJIMP estimated primaries. Panel (e): LSJIMP estimated multiples. morgan1-comp.radon.gc3d.100 [CR]

the model regularization operators also exploit moveout differences to separate multiples and primaries.

Figure **??**, a stack of the LSHRTD estimated primaries, can be compared directly with the LSJIMP result, Figure **??**. Like before, the multiples predominantly stack out, since the moveout separation is so significant. Still, a noticeable amount of multiple energy has been removed by LSHRTD, perhaps more than by LSJIMP. However, we immediately see some removed primary energy: for example, the strong primary near the bottom of the section.

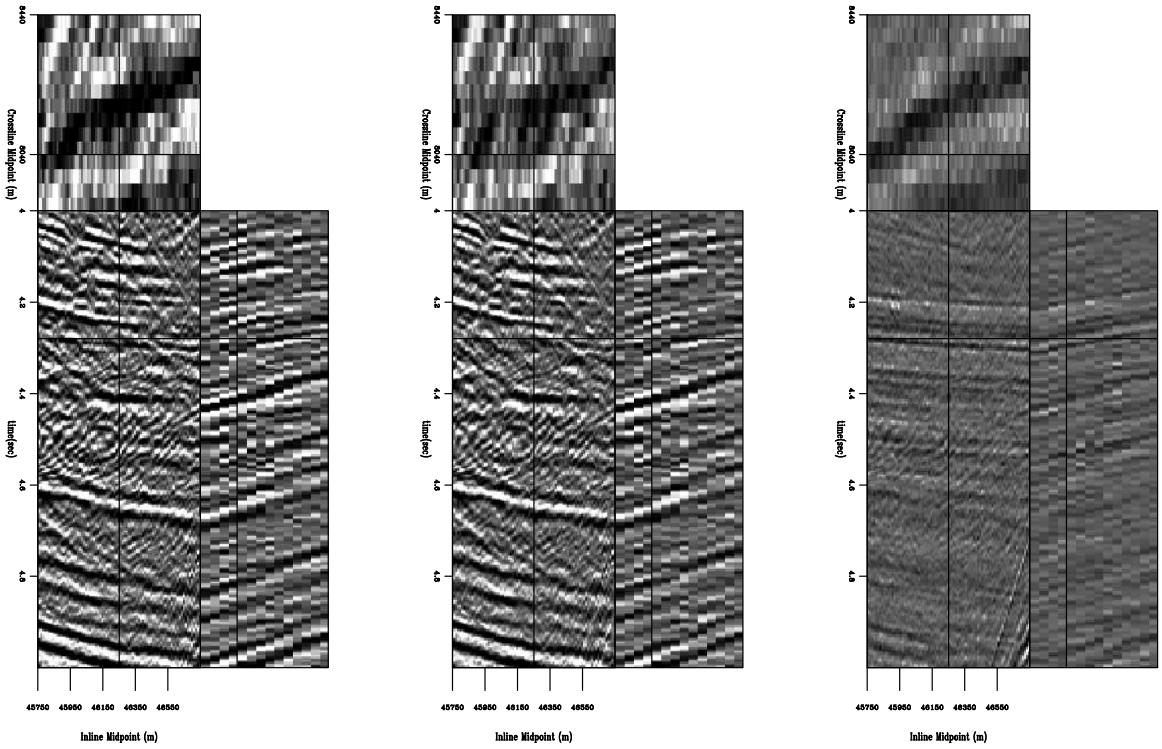

Figure 11: NMO/Stack comparison before and after LSHRTD. Compare directly with Figure **??**. Left: Raw data. Center: LSHRTD estimated primaries. Right: difference. morgan1-stackcomp3d.radon.zoom.gc3d [CR,M]

AVO Analysis Before and After LSJIMP

Amplitude-versus-offset or AVO analysis is perhaps the most commonly utilized direct hydrocarbon indicator in exploration reflection seismology today. The stacked results before and after LSJIMP on the Green Canyon 3-D dataset showed that stacking greatly attenuates multiples. However, from the prestack data, we saw that the multiples are prominent, and would surely inhibit signal processing techniques, like AVO analysis, if left intact. In this section, I illustrate how LSJIMP improves the AVO analysis of the Green Canyon 3-D data.

Shuey (1985) showed that in a 1-D earth, the measured reflection strength of an event at the surface is approximately linear with the square of its incidence angle, at angles less than 30

degrees. In a 1-D earth, the NMO equation gives an approximate relationship between offset and incidence angle. Claerbout (1995) defines the "stepout", p, as the spatial derivative of an event's traveltime curve:

$$p = \frac{dt}{dx} = \frac{\sin\theta}{V}, \tag{9}$$

where θ is the incidence angle and V is the velocity at the surface; in the marine case, simply water velocity. In a 1-D earth, the traveltime curve of a primary reflection is approximately given by the NMO equation. Taking its derivative with respect to offset, then substituting into equation (9) gives the following expression for the sine of incidence angle as a function of offset:

$$\sin\theta = \frac{V}{V^2_{\rm rms}(\tau)} \frac{x}{\sqrt{\tau^2 + \frac{x^2}{V^2_{\rm rms}(\tau)}}}. \tag{10}$$

Reflection data as a function of offset may be mapped to $\sin^2\theta$ via equation (10), at which point the AVO "slope" and "intercept" parameters may be estimated, usually via a linear least-squares fit to the data after resampling from offset to $\sin^2\theta$.

Figure **??** illustrates the estimation of AVO slope and intercept parameters on a deep reflector in the Green Canyon 3-D data, before and after application of LSJIMP. The reflector, which is well under the multiples in the data, is denoted on the zero offset section with "O" symbols. The maximum amplitude in a small time window around the reflection were picked automatically, and make up the input data to the least-squares estimation.

We see that while the parameter estimates contain the same trends before and after LSJIMP, the LSJIMP result is more consistent and less "noisy" across midpoint. My implementation of LSJIMP works on a CMP-by-CMP basis, so the results shown in Figure **??** are not smoothed across midpoint. The similarity across midpoint is an expression of the true lithology – lithology which LSJIMP better reveals.

Figure **??** illustrates, as a function of midpoint, the small time windows taken around the deep reflector shown in Figure **??**, before and after LSJIMP. The input data to an AVO parameter estimation are picked maximum amplitudes within the time window as a function of $\sin^2\theta$. Notice the significant increase in reflector clarity after LSJIMP. Also recall that the data residuals (e.g., in Figures **??** and **??**) are quite small. Therefore, the cleaner reflection events after LSJIMP in Figure **??** are not only better for AVO analysis – they also fit the recorded data in a quantitative fashion. LSJIMP is not an *ad hoc* post-processing technique.

CONCLUSIONS

On the CGG Green Canyon 3-D dataset, LSJIMP again demonstrated an excellent ability to separate primaries and multiples. The data subset shown in the paper came from a sedimentary minibasin, which boasts a simple velocity profile, high signal-to-noise ratio, and fairly mild (but non-trivial) dips. The full dataset released by CGG contains much data recorded over

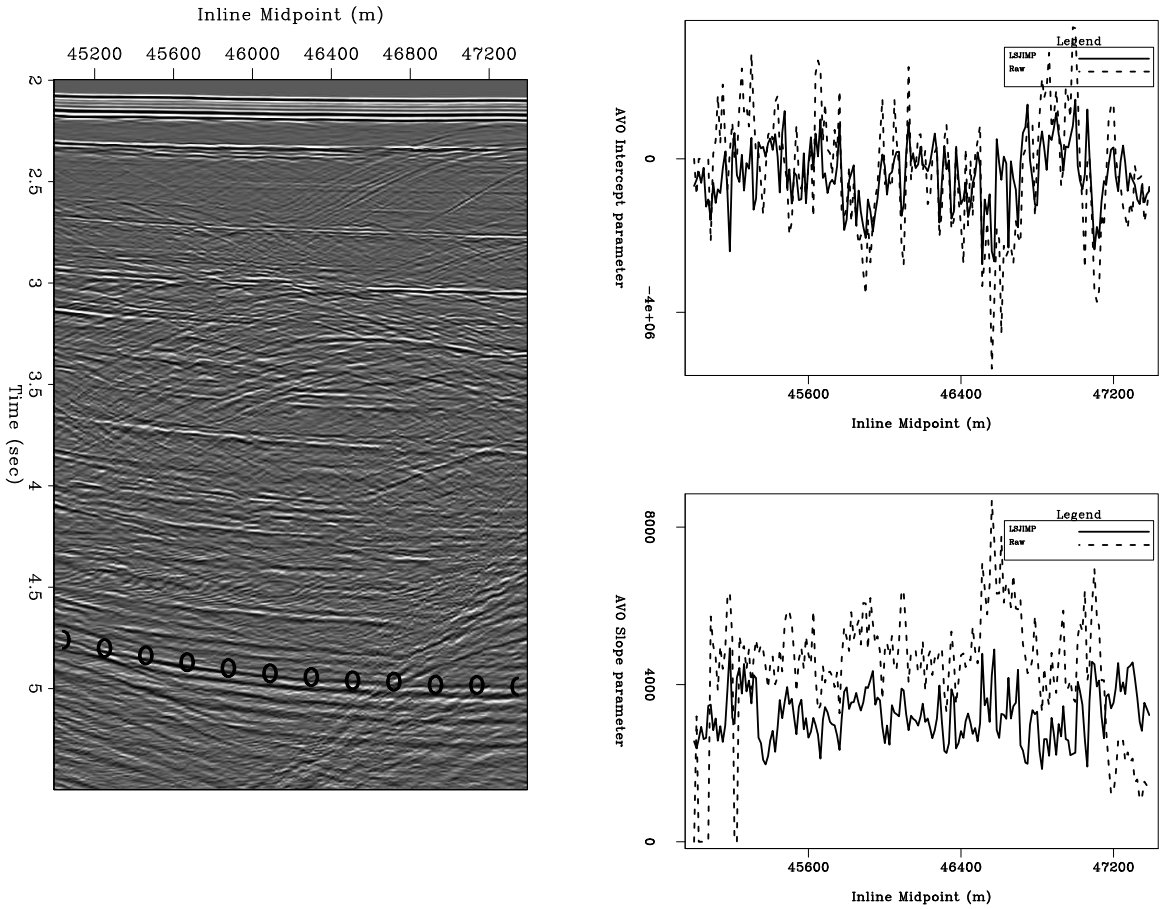

Figure 12: AVO parameter estimation for a deep reflector. Left: zero offset section, "O" symbols denote reflector of interest. Right, top: AVO intercept parameter before and after LSJIMP, as a function of midpoint. Right, bottom: AVO slope parameter before and after LSJIMP, as a function of midpoint. morgan1-maxampl.gc3d.4-5 [CR]

salt. In preliminary tests on one salt region, NMO and HEMNO proved unable to correctly image primaries or multiples. The salt bodies often exhibit crossline dips of over 30 degrees, which, when combined with the data's inherent sparsity, severely test even the most advanced imaging techniques.

The data subset is particularly well-suited for Radon demultiple, with its large velocity gradient and gentle geology. I tested least-squares hyperbolic Radon demultiple (LSHRTD) and found that LSJIMP compares quite favorably, both in terms of computational efficiency, multiple separation, and amplitude preservation.

A quantitative study of prestack reflection amplitudes confirmed what was suspected; LSJIMP's ability to remove multiples and random noise, as well as its ability to use multiples and other constraints to interpolate missing traces, improves prestack amplitude analysis.

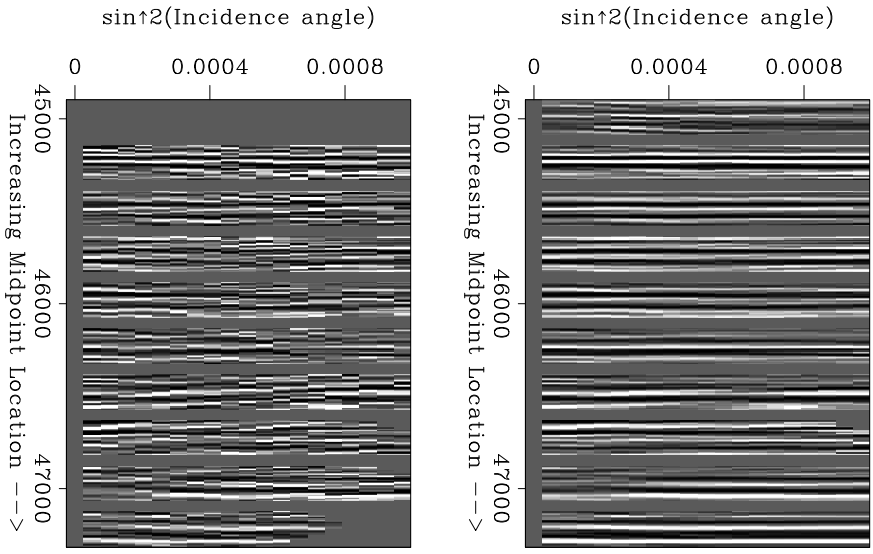

Figure 13: Small time windows around the deep reflector shown in Figure **??**, before and after LSJIMP. Individual panels along the vertical axis correspond to windows taken at different midpoint locations. Left: Data windows before LSJIMP. Right: Data windows after LSJIMP. morgan1-avogather.gc3d.4-5 [CR]

REFERENCES

Biondi, B., and Palacharla, G., 1996, 3-D prestack migration of common-azimuth data: Geophysics, **61**, no. 06, 1822–1832.

Biondi, B., Fomel, S., and Chemingui, N., 1998, Azimuth moveout for 3-D prestack imaging: Geophysics, **63**, no. 02, 574–588.

Biondi, B., 1997, Azimuth moveout + common-azimuth migration: Cost-effective prestack depth imaging of marine data: Soc. of Expl. Geophys., 67th Ann. Internat. Mtg, 1375–1378.

Brown, M., and Guitton, A., 2004, Efficient prestack modeling and imaging of pegleg multiples: 74th Ann. Internat. Mtg., Soc. of Expl. Geophys., Expanded Abstracts, submitted.

Brown, M., 2003a, Amplitude modeling of pegleg multiple reflections: SEP–**113**, 97–106.

Brown, M., 2003b, Least-squares joint imaging of primaries and pegleg multiples: 2-D field data test: SEP–**113**, 17–30.

Brown, M., 2003c, Prestack time imaging operator for 2-D and 3-D pegleg multiples over nonflat geology: SEP–**113**, 85–96.

Claerbout, J. F., 1995, Basic Earth Imaging: Stanford Exploration Project.

Foster, D. J., and Mosher, C. C., 1992, Suppression of multiple reflections using the Radon transform: Geophysics, **57**, no. 03, 386–395.

Hampson, D., 1986, Inverse velocity stacking for multiple elimination: J. Can. Soc. Expl. Geophys., **22**, no. 01, 44–55.

Kabir, M. M. N., and Marfurt, K. J., 1999, Toward true amplitude multiple removal: The Leading Edge, **18**, no. 1, 66–73.

Sacchi, M. D., and Ulrych, T. J., 1995, High-resolution velocity gathers and offset space reconstruction: Geophysics, **60**, no. 04, 1169–1177.

Shuey, R. T., 1985, A simplification of the Zoeppritz-equations: Geophysics, **50**, no. 04, 609–614.

Thorson, J. R., and Claerbout, J. F., 1985, Velocity stack and slant stochastic inversion: Geophysics, **50**, no. 12, 2727–2741.

van Dedem, E., and Verschuur, D., 2002, 3D surface-related multiple prediction using sparse inversion: experience with field data: Soc. of Expl. Geophys., 72nd Ann. Internat. Mtg, 2094–2097.